ELSEVIER

Computer Physics Communications 87 (1995) 319–340

Computer Physics Communications

A hybrid decomposition parallel implementation of the Car–Parrinello method

James Wiggs, Hannes Jónsson

Department of Chemistry, BG-10, University of Washington, Seattle, WA 98195, USA

Received 17 July 1994

Abstract

We have developed a flexible hybrid decomposition parallel implementation of the first-principles molecular dynamics algorithm of Car and Parrinello. The code allows the problem to be decomposed either spatially, over the electronic orbitals, or any combination of the two. Performance statistics for 32, 64, 128 and 512 Si atom runs on the Touchstone Delta and Intel Paragon parallel supercomputers and comparison with the performance of an optimized code running the smaller systems on the Cray Y-MP and C90 are presented.

1. Introduction

The ab initio molecular dynamics technique of Car and Parrinello [1,2] has become a valuable method for studying condensed matter structure and dynamics, in particular liquids [3–6], surfaces [7–9], and clusters [10–12]. In a Car–Parrinello (CP) simulation the electron density of the ground electronic state is calculated within the local density approximation (LDA) of density functional theory (DFT), and is used to calculate the forces acting on the ions. The electronic orbitals are expanded in a plane-wave basis set; a classical Lagrangian linking the ionic coordinates with the expansion coefficients is then used to generate a coupled set of equations of motion describing the extended electron–ion system. The motion of the electrons can be often adjusted so that they follow the motion of the ions adiabatically, remaining close to the Born–Oppenheimer ground state as the system evolves. Thus the ions move according to ab initio forces determined directly from the electronic ground state at each time step, rather than from an empirical potential. As such, the CP algorithm overcomes many of the limitations of standard empirical-potential approaches, such as transferability of potentials and, furthermore, provides direct information about the electronic structure. However, CP simulations are computationally demanding and systems larger than $\sim$ 100 atoms can not be simulated in a reasonable amount of time on traditional vector supercomputers. Furthermore, the memory requirements for simulations of large systems easily exceed the available memory on shared-memory supercomputers.

Many systems of interest require simulations of 10^3 atoms as is commonly done in molecular dynamics simulations with empirical potentials. In order to study larger systems with the CP approach it is necessary to take advantage of the computing power and memory available on parallel supercomputers. A parallel supercomputer can offer a considerable increase in performance over traditional vector supercomputers by

Elsevier Science B.V.
SSDI 0010-4655(94)00153-7

replacing the small number of processors sharing a single memory space (e.g. the Cray C-90) with a large number of computing nodes, each consisting of a slower – but much less expensive – processor with its own memory. The nodes have some means of communicating data with one another to work cooperatively when solving the problem. An efficient use of parallel computers requires that a significant fraction of the computation can be done in an arbitrary order, such that tasks can be done simultaneously on the individual nodes without excessive data communication between the nodes.

Several groups have implemented the CP algorithm [13–16] or similar plane-wave electronic-structure calculations [17] on parallel supercomputers. A large fraction of the computation in such calculations involves fast Fourier transforms (FFT). Most groups [13–15,17] have used a spatial decomposition of the problem where each node was made responsible for calculations on a subset of the plane-wave coefficients used to describe each orbital, basically implementing a parallel FFT. This allows efficient implementation of calculations involving several different orbitals, most importantly the orthonormalization of the orbitals and the non-local portion of the Hamiltonian. However, it is quite difficult to implement domain-decomposition multi-dimensional FFTs efficiently, particularly on parallel computers with low degrees of connectivity such as the mesh-connection [18–20] due to the communication requirements. This seriously reduces the efficiency when calculating the electronic density and the action of the local part of the Hamiltonian. Alternatively, we chose an orbital decomposition where each node was made responsible for *all* the expansion coefficients for a subset of the *orbitals* [16]. This approach has advantages and disadvantages when compared with the spatial decomposition. Much of the computation involves independent operations on the orbitals such as the FFT, and the orbital decomposition makes it possible to do them fully in parallel without any communication between nodes. One disadvantage of the orbital decomposition is that the orthonormalization requires extensive communication between nodes; another disadvantage of the orbital decomposition when applied to large problems is the requirement that each node set aside memory for the entire three-dimensional FFT lattice, rather than storing only a small portion of it.

As more and more nodes are applied to the calculation, a point of diminishing returns is reached in both cases. There are irreducible minimum amounts of communication, redundant computation done on each node to avoid communication, synchronization, and load-balancing problems which all act together to limit the efficiency of any parallel implementation. In order to apply the CP algorithm to large problems, and to make optimal use of parallel computers, we have developed a code which can use a *combination* of the orbital and spatial decomposition. This relieves the memory limitations of the orbital decomposition, and makes it possible to balance out the losses in efficiency for different parts of the computation so as to get *optimal* speedup for a given number of nodes. We present here results of tests on this code on different sized problems. We find that the optimal decomposition in every case we studied was neither purely spatial nor purely orbital, but rather a combination of the two.

2. The CP algorithm

The CP algorithm describes a system of interacting ions and electronic orbitals with the classical Lagrangian [1–3]

$$L=\sum_{n}^{N}\mu f_n\int_{\Omega}\mathrm{d}\boldsymbol{r}\,|\dot{\psi}_n(\boldsymbol{r})|^2+\frac{1}{2}\sum_{I}M_I\dot{\boldsymbol{R}}_I^2-E[\{\boldsymbol{R}_I\},\{\psi_n\}]+\sum_{n,m}\Lambda_{nm}\left(\int\mathrm{d}\boldsymbol{r}\,\psi_n^*(\boldsymbol{r})\psi_m(\boldsymbol{r})-\delta_{nm}\right), \quad (2.1)$$

where the $\{\boldsymbol{R}_I\}$ are the ionic coordinates and the M_I their masses, dots indicate time derivatives, Ω is the volume of the simulation cell, $\int_{\Omega}$ indicates integration over the simulation cell, μ is a fictitious mass associated with the time-dependent electronic orbitals to control the time scale of the electronic motion (typically $\mu \ll M_I$)

and E is energy functional of the system within the DFT. The Λ_{nm} are Lagrange multipliers which impose orthonormality constraints on the electronic orbitals ψ_n:

$$\langle \psi_n | \psi_m \rangle = \int \mathrm{d}\boldsymbol{r}\ \psi_n^*(\boldsymbol{r}) \psi_m(\boldsymbol{r}) = \delta_{nm}\,, \tag{2.2}$$

where the δ_{nm} is the standard Kronecker delta function, equal to one when $n = m$ and zero otherwise. The classical equations of motion are derived from the Lagrangian in the usual way:

$$\mu \ddot{\psi}_n(\boldsymbol{r},t) = -\frac{1}{2} \frac{\delta E}{\delta \psi_n^*(\boldsymbol{r},t)} + \sum_m \Lambda_{nm} \psi_m(\boldsymbol{r},t) \tag{2.3}$$

and

$$M_I \ddot{\boldsymbol{R}}_I = -\frac{\partial E}{\partial \boldsymbol{R}_I(t)}. \tag{2.4}$$

The DFT energy functional [21,22] has the form

$$E[\{\boldsymbol{R}_I\},\{\psi_n\}] = \sum_n^N f_n \int \mathrm{d}\boldsymbol{r}\ \psi_n^*(\boldsymbol{r})(-\tfrac{1}{2}\nabla^2)\ \psi_n(\boldsymbol{r}) + \int \mathrm{d}\boldsymbol{r}\ V^{\mathrm{ext}}(\boldsymbol{r})\ \rho(\boldsymbol{r})$$
$$+ \frac{1}{2} \int \mathrm{d}\boldsymbol{r}\,\mathrm{d}\boldsymbol{r}'\ \frac{\rho(\boldsymbol{r})\rho(\boldsymbol{r}')}{|\boldsymbol{r}-\boldsymbol{r}\prime|} + E^{\mathrm{xc}}[\rho] + \frac{1}{2} \sum_{I \neq J} \frac{Z_I Z_J}{|\boldsymbol{R}_I - \boldsymbol{R}_J|}, \tag{2.5}$$

where $\rho(\boldsymbol{r})$ is the electron density at $\boldsymbol{r}$, $E^{\mathrm{xc}}[\rho]$ is the LDA of the exchange-correlation energy for electronic density ρ, f_n is the occupation number of orbital ψ_n, Z_I is the valence charge of atom I, and $V^{\mathrm{ext}}(\boldsymbol{r})$ is a sum of ionic pseudopotentials. We use the angular-momentum dependent, norm-conserving pseudopotentials of Bachelet, Hamann, and Schlüter (BHS) [23] in the factorized form of Kleinman and Bylander [24] for the nonlocal parts. The electron density $\rho(\boldsymbol{r})$ is expressed in terms of the N orbitals ψ_n

$$\rho(\boldsymbol{r}) = \sum_n^N f_n\ |\psi_n(\boldsymbol{r})|^2. \tag{2.6}$$

If the functional $E[\{\boldsymbol{R}_I\},\{\psi_n\}]$ is minimized with respect to the electronic orbitals for fixed ionic positions, the BO potential surface for the ions, $\Phi[\{\boldsymbol{R}_I\}]$, is obtained. The equations of motion derived from Eq. (2.1) make it possible to optimize simultaneously the electronic and ionic degrees of freedom using, for example, steepest descent (SD) minimization. Furthermore, they allow one to perform finite-temperature molecular dynamics on the BO potential surface once the electronic degrees of freedom have been minimized. Under favorable conditions the value of μ can be chosen such that the electronic orbitals can remain close to the BO surface as the ionic coordinates evolve according to Eq. (2.4). When doing finite-temperature simulations of metallic systems, it is often necessary to periodically re-quench the electronic orbitals to the BO surface by holding the ions fixed and performing SD or conjugate gradient (CG) minimization on the electrons according to Eq. (2.3). The temperature of the ions can be controlled by any convenient thermostat, such as velocity scaling, stochastic collisions[25], or the Nosé–Hoover thermostat [26,27].

3. Numerical implementation

The CP algorithm is most easily applied by expanding the electronic orbitals in sums of plane waves:

$$\psi_{n,k}(\boldsymbol{r}) = \exp(\mathrm{i}\boldsymbol{k}\cdot\boldsymbol{r}) \sum_g c_g^n \exp(\mathrm{i}\boldsymbol{g}\cdot\boldsymbol{r}), \tag{3.1}$$

where the g's are reciprocal lattice vectors of the simulation cell:

$$g = n_x \frac{2\pi}{a_x}\hat{x} + n_y \frac{2\pi}{a_y}\hat{y} + n_z \frac{2\pi}{a_z}\hat{z}, \tag{3.2}$$

where a_x, a_y, and a_z are the dimensions of the simulation cell, n_x, n_y, and n_z can have any integer value and $\hat{x}$, $\hat{y}$, and $\hat{z}$ are the unit vectors in the x, y, and z directions. The expression is simple in this case due to the fact that our simulation cell has all internal angles equal to 90 degrees. Other simulation cell symmetries can be used, but result in a more complex expression for the reciprocal lattice vector's basis set. The set of g is limited to those whose kinetic energy $E_{\rm kin} = \frac{1}{2}|g|^2$ is less than some energy cutoff $E_{\rm cut}$; a larger value of $E_{\rm cut}$ increases the accuracy of the expansion. The number of such g is hereafter referred to as M. A typical value of $E_{\rm cut}$ for a simulation of silicon is about 12.0 Rydbergs ($\simeq$ 163 eV). In principle, several k vectors need to be included to sample the first Brillouin zone; however, this becomes less and less important as the size of the simulation cell is increased. Since we were primarily interested in simulating large systems with our parallel code the only k-point included is $(0,0,0)$, the Γ point. This choice of basis set forces the orbitals to have the same periodicity as the simulation cell when periodic boundary conditions are applied. It has the additional benefit of making the phase of the wavefunction arbitrary; we can therefore choose it to be real, which is equivalent to stating that $c_{-g} = c_g^*$, which reduces the required storage for the expansion coefficients by a factor of two.

The plane wave expansion has the added benefit that certain parts of the Hamiltonian are very easily calculated in terms of the g's, i.e. in reciprocal space. While other parts of the calculation are more efficiently carried out in real space, the plane wave basis makes it possible to switch quickly from reciprocal space to real space and back using FFTs. This reduces the work required to calculate the functional derivatives in Eq. (2.3) from $O(NM^2)$ to $O(NM \log M)$, making the most computationally expensive portion of the calculation the imposition of orthonormality and the Kleinman-Bylander nonlocal pseudopotentials, which require $O(N^2M)$ computation. Any parallel implementation of the algorithm will have to perform these parts of the calculation efficiently to achieve good speedup.

3.1. The pseudopotential calculation

Introduction of pseudopotentials not only reduces the number of electrons included in the calculation by allowing us to treat only the valence electrons, it also greatly reduces the size of the basis set required to accurately describe the wavefunctions and the electron density and potential since it is not necessary to reproduce the fine structure in the regions of space near the nuclei. The Kleinman-Bylander factorized form of the pseudopotentials first describes the interaction of the valence electrons with the ionic cores as a sum of ionic pseudopotentials

$$V(r) = \sum_I v_{\rm ps}(r - R_I), \tag{3.3}$$

then breaks these pseudopotentials down further into sums of angular-momentum dependent potentials

$$v_{\rm ps}(r) = \sum_{l=0}^{\infty} v_l(r)\hat{P}_l, \tag{3.4}$$

where $\hat{P}_l$ projects out the lth angular momentum. The assumption is made that for some $l > l_{\rm max}$, $v_l(r) = v_{l_{\rm max}}(r)$. For most elements, this approximation is good for $l_{\rm max} = 1$ *or* 2. Since $\hat{P}_l$ is a complete set, Eq. (3.4) can be written as

$$v_{\rm ps}(r) = v_{\rm loc}(r) + \sum_{l=0}^{l_{\rm max}-1} \delta v_l(r)\hat{P}_l, \tag{3.5}$$

with

$$\delta v_l(r) = v_l(r) - v_{l_{\max}}(r). \tag{3.6}$$

The Kleinman–Bylander formalism then replaces the sum in Eq. (3.5) with a fully nonlocal potential:

$$\tilde{v}_{\rm nl}(r) = \sum_{l,m} \frac{|\delta v_l \Phi^0_{l,m}\rangle\langle\Phi^0_{l,m}\delta v_l|}{\langle\Phi^0_{l,m}|\delta v_l|\Phi^0_{l,m}\rangle}, \tag{3.7}$$

where $\Phi^0_{l,m} = \phi_l Y_{lm}$, with Y_{lm} being the spherical harmonic and ϕ_l the lth atomic pseudowavefunction from which the v_l were originally generated. In the plane-wave implementation, if we make the following definitions:

$$u_l(g) = \int {\rm d}r\, r^2 j_l(gr)\delta v_l(r)\phi_l(r), \tag{3.8}$$

$$W_l = \int {\rm d}r\, r^2 j_l(r)\delta v_l(r)\phi_l(r)^2, \tag{3.9}$$

then it can be shown that the matrix element of the nonlocal part of the Hamiltonian in reciprocal space is

$$\langle g|\tilde{v}_{\rm nl}|g'\rangle = \frac{4\pi}{\Omega}\sum_l \frac{(2l+1)P_l(cos(\theta_{g,g'}))}{W_l} u_l(g)u_l(g'). \tag{3.10}$$

The forces on the electronic coefficients due to their interaction with the ions is

$$\frac{\partial \tilde{v}^l_{\rm nl}(g)}{\partial c^n_g} = 2\frac{\sum_I \exp(-{\rm i}g\cdot R_I)u_l(g)F^{\rm In}_l}{W_l}, \tag{3.11}$$

where

$$F^{\rm In}_l = \sum_g^M u_l(g)\exp({\rm i}g\cdot R_I)c^n_g. \tag{3.12}$$

Calculating the $F^{\rm In}_l$ is the most computationally demanding part of the pseudopotential calculation, requiring $O(N^2M)$ work. It should be noted that implementations of the non-local pseudopotentials calculated in real space have been suggested [29,30] which would reduce the scaling of this calculation to $O(N^2)$, but with a large prefactor. Such techniques could be efficiently implemented within our hybrid parallel code, reducing the scaling of this portion of the calculation to $O(N)$ when the number of processors is increased with the number of atoms, but we have not yet done so.

3.2. The orthonormalization

The orthonormality of the electronic orbitals may be maintained in two ways: either by a straightforward technique like Gram–Schmidt (GS) orthonormalization or by an iterative technique as given by Car and Parrinello [2] based upon the more general method for imposing holonomic constraints described by Ryckaert et al. [28]. Both techniques have been implemented in our code, but the iterative technique is preferred when doing ionic dynamics.

Applying the functional derivatives in Eq. (2.3) to the $\{\psi_n\}$, produces a new, non-orthonormal set $\{\bar{\psi}_n\}$. This set can be brought to orthonormality using the real symmetric matrix $\mathbf{X} = ((\delta t)^2/\mu)\Lambda$. $\mathbf{X}$ can be recovered by first defining the matrices $\mathbf{A}$ and $\mathbf{B}$ as

$$A_{nm} = \langle\bar{\psi}_n|\bar{\psi}_m\rangle, \tag{3.13}$$

$$B_{nm} = \langle \psi_n | \bar{\psi}_m \rangle, \tag{3.14}$$

then making a first order approximation to $\mathbf{X}$ with

$$\mathbf{X}^{(0)} = \tfrac{1}{2}(\mathbf{I} - \mathbf{A}) \tag{3.15}$$

and iterating

$$\mathbf{X}^{(k)} = \tfrac{1}{2}[\mathbf{I} - \mathbf{A} + \mathbf{X}^{(k-1)}(\mathbf{I} - \mathbf{B}) + (\mathbf{I} - \mathbf{B})^T \mathbf{X}^{(k-1)} - \mathbf{X}^{(k-1)^2}], \tag{3.16}$$

until

$$\text{Max}|X_{nm}^{(k)} - X_{nm}^{(k-1)}| < \epsilon. \tag{3.17}$$

The value of ϵ determines how close to orthonormal the orbitals remain and how many iterations of Eq. (3.16) are required to achieve orthonormality. A typical value of 10^{-6} generally requires less than four iterations.

In a plane wave basis set, with Γ point symmetry, it can be shown that the overlap of two wavefunctions is

$$\langle \psi_n | \psi_m \rangle = \frac{1}{\Omega} \int_{\Omega} \mathrm{d}\boldsymbol{r}\, \psi_n^*(\boldsymbol{r}) \psi_m(\boldsymbol{r}) = \mathrm{Re}[c_0^n] \cdot \mathrm{Re}[c_0^m] + 2 \sum_{g \neq 0}^{M} (\mathrm{Re}[c_g^n] \cdot \mathrm{Re}[c_g^m] + \mathrm{Im}[c_g^n] \cdot \mathrm{Im}[c_g^m]) \tag{3.18}$$

so that calculating each element $\mathbf{A}$ and $\mathbf{B}$ reduces to doing slightly modified dot product, and thus calculating $\mathbf{A}$ and $\mathbf{B}$ requires multiplying one $M \times N$ matrix of expansion coefficients by another matrix with dimension $N \times M$. An operation requiring $O(N^2 M)$ computation. It is possible to exploit certain matrix properties, store intermediate values of some matrices, and define the iteration matrix somewhat differently, so that the number of multiplications in the iteration loop is reduced to one. Since these are multiplications of $N \times N$ matrices, requiring $O(N^3)$ computation, and $M \gg N$, the overall time is reduced, but only marginally. The calculations required, in a plane wave basis set, reduce to

$$\begin{aligned} 2X_{nm}^0 &= \delta_{nm} + \mathrm{Re}[\bar{c}_0^n(t+\delta t)] \cdot \mathrm{Re}[\bar{c}_0^m(t+\delta t)] \\ &\quad - \sum_g^M \left(\mathrm{Re}[\bar{c}_g^n(t+\delta t)] \cdot \mathrm{Re}[\bar{c}_g^m(t+\delta t)] + \mathrm{Im}[\bar{c}_g^n(t+\delta t)] \cdot \mathrm{Im}[\bar{c}_g^m(t+\delta t)]\right), \end{aligned} \tag{3.19}$$

$$\begin{aligned} b_{nm} &= \delta_{nm} + \mathrm{Re}[c_0^n(t)] \cdot \mathrm{Re}[\bar{c}_0^m(t)] \\ &\quad - \sum_g^M \left(\mathrm{Re}[c_g^n(t)] \cdot \mathrm{Re}[\bar{c}_g^m(t+\delta t)] + \mathrm{Im}[c_g^n(t)] \cdot \mathrm{Im}[\bar{c}_g^m(t+\delta t)]\right), \end{aligned} \tag{3.20}$$

$$X^{(k)} = X^{(0)} + X^{(k-1)} b + b^T X^{(k-1)} - X^{(k-1)^2}, \tag{3.21}$$

$$c_g^n(t+\delta t) = \bar{c}_g^n(t+\delta t) + \sum_{m=1}^{N} X_{nm}^{(k)} c_g^m(t), \tag{3.22}$$

3.3. Summary of the computational modules

A schematic summary of the evaluation of the force on the electronic coefficients is given in Table 1. Over 90 % of the numerical computation is spent in dealing with the electronic degrees of freedom; it breaks down into six major tasks. Below is a description of the work involved in each task.

rhoofr involves calculation of the total electronic density $\rho(\boldsymbol{r})$ in the simulation cell (Eq. (2.6)).

Table 1
Operations in the Car–Parrinello algorithm for N orbitals (indexed with n) and M plane waves (indexed with g)

Task	Operations
rhoofr	$c_{\boldsymbol{g}}^{n} \xrightarrow{\text{FFT}} \Psi_n(\boldsymbol{r})$ $\rho(\boldsymbol{r}) = \sum_n^N 2\,\lvert\Psi_n(\boldsymbol{r})\rvert^2$
vofrho	$\rho(\boldsymbol{r}) \xrightarrow{\text{FFT}} \rho(\boldsymbol{g})$ $\tilde{v}(\boldsymbol{g}) = (4\pi/\lvert\boldsymbol{g}\rvert^2)\ \rho(\boldsymbol{g}) + v_{\text{loc}}(\boldsymbol{g})$ $\tilde{v}(\boldsymbol{g}) \xrightarrow{\text{FFT}} \tilde{v}(\boldsymbol{r})$ $v(\boldsymbol{r}) = \tilde{v}(\boldsymbol{r}) + \mu_{xc}(\rho(\boldsymbol{r}))$
nonlocal	$F_I^{ln} = \sum_{\boldsymbol{g}}^{M} u_l(\boldsymbol{g}) \exp(\mathrm{i}\boldsymbol{g}\cdot\boldsymbol{R}_I)\, c_{\boldsymbol{g}}^{n}$ $\partial\tilde{v}_{\text{nl}}^{l}(\boldsymbol{g})/\partial c_{\boldsymbol{g}}^{n} = 2(W_l)^{-1}\sum_I \exp(-\mathrm{i}\boldsymbol{g}\cdot\boldsymbol{R}_I) u_l(\boldsymbol{g}) F_I^{ln}$ $\partial E/\partial c_{\boldsymbol{g}}^{n} = \partial\tilde{E}/\partial c_{\boldsymbol{g}}^{n} + \sum_{l=0}^{l_m} \partial\tilde{v}_{\text{nl}}^{l}(\boldsymbol{g})/\partial c_{\boldsymbol{g}}^{n}$
local	$c_{\boldsymbol{g}}^{n} \xrightarrow{\text{FFT}} \Psi_n(\boldsymbol{r})$ $2\Psi_n(\boldsymbol{r})\ v(\boldsymbol{r}) \xrightarrow{\text{FFT}} \partial\tilde{E}/\partial c_{\boldsymbol{g}}^{n}$
loop	$\bar{c}_{\boldsymbol{g}}^{n}(t+\delta t) = -c_{\boldsymbol{g}}^{n}(t-\delta t) + 2c_{\boldsymbol{g}}^{n}(t) - [(\delta t)^2/\mu]\ \partial E/\partial c_{\boldsymbol{g}}^{n}$
ortho	$2X_{nm}^{(0)} = \delta_{nm} - \sum_{\boldsymbol{g}}^{M} \bar{c}_{\boldsymbol{g}}^{n*}(t+\Delta t)\ \bar{c}_{\boldsymbol{g}}^{m}(t+\Delta t)$ $b_{nm} = \delta_{nm} - \sum_{\boldsymbol{g}}^{M} c_{\boldsymbol{g}}^{n*}(t)\ \bar{c}_{\boldsymbol{g}}^{m}(t+\Delta t)$ $X^{(k)} = X^{(0)} + X^{(k-1)}b + b^T X^{(k-1)} - X^{(k-1)^2}$ $c_{\boldsymbol{g}}^{n}(t+\Delta t) = \bar{c}_{\boldsymbol{g}}^{n}(t+\Delta t) + \sum_{m=1}^{N} X_{nm}^{(k)} c_{\boldsymbol{g}}^{m}(t)$

vofrho uses the total electronic density generated by **rhoofr** to determine the total local electronic potential as a function of $\rho(\boldsymbol{r})$ throughout the simulation cell, including the contribution of the electron exchange-correlation potential and Hartree interactions (Eq. (2.5)), and the *local* portion of the pseudopotential (Eq. (3.5)). The pseudopotential and the Hartree interactions are determined in reciprocal space; the exchange-correlation potential in real space.

nonlocal determines the portion of the unconstrained functional derivatives of the electronic coefficients due to the nonlocal portion of the pseudopotential, using the Kleinman-Bylander factorized form (Eq. (3.11)). In addition, when doing ionic dynamics, it calculates the force exerted on the ions by the electrons, interacting through the nonlocal pseudopotential.

local determines the portion of the unconstrained functional derivatives of the electronic coefficients due to the total local potential calculated in **vofrho**.

loop updates the sets of electronic coefficients according to these unconstrained functional derivatives:

$$\bar{c}_{\boldsymbol{g}}^{n}(t+\delta t) = -c_{\boldsymbol{g}}^{n}(t-\delta t) + 2c_{\boldsymbol{g}}^{n}(t) - \frac{(\delta t)^2}{\mu}\frac{\partial E}{\partial c_{\boldsymbol{g}}^{n}}, \tag{3.23}$$

where $\bar{c}_{\boldsymbol{g}}^{n}(t+\delta t)$ are the new set of expansion coefficients *before application of the constraint forces*.

Orthonormalization is carried out either in **ortho** via calculation and application of constraint forces, or in **gram** via the simple Gram–Schmidt procedure.

4. Parallel implementation

Table 1 gives a schematic representation of the CP algorithm. It suggests two approaches to the parallel implementation. It is noted that the work on each electronic orbital ψ_n is largely independent of the work

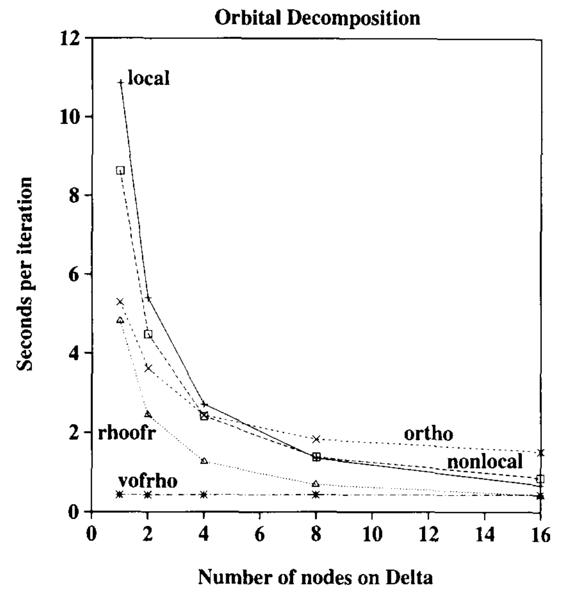

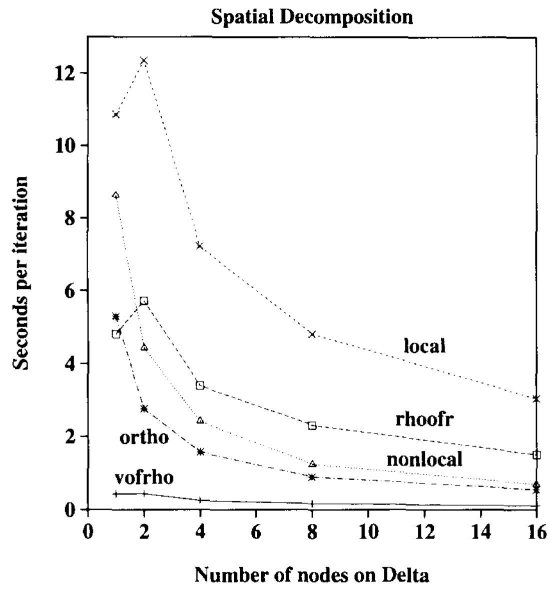

Fig. 1. CPU time for major tasks in a pure orbital decomposition parallel Car–Parrinello simulation of 32 Si atoms at a 12 Ry cutoff energy. Efficiently parallel tasks should require approximately half the processing time when the number of nodes is doubled. Examples of this are **rhoofr** and **local**

Fig. 2. CPU time for major tasks in a purely spatial decomposition parallel Car–Parrinello simulation of 32 Si atoms at a 12 Ry cutoff energy. Efficiently parallel tasks should require approximately half the processing time when the number of nodes is doubled. Examples of this are **nonlocal** and **ortho**

done on the other electronic orbitals; this implies that dividing the orbitals up among the nodes, an orbital decomposition, may be successful, and in fact this proves to be the case [16]. This type of parallelism is often referred to as coarse-grain or macro-tasking parallelism; the amount of work assigned to each node is quite large, and the number of nodes which can be applied to the problem is limited. Closer examination suggests that the work done on each expansion coefficient c_g^n is also independent of the work done on the other coefficients. For example **loop**, the second and third subtask of **nonlocal**, and the second subtask in **vofrho**. This implies that we might divide up the coefficients among the nodes, an example of fine-grain or micro-tasking parallelism, the approach usually favored by parallelizing compilers. The number of nodes which can be applied to the problem in this manner is theoretically limited only by the number of coefficients, but effectively the limit is much smaller due to load balancing and communications requirements in some parts of the code. This spatial decomposition approach has been utilized by several groups [13–15,17].

Each approach has advantages and drawbacks. Fig. 1 shows the time spent doing various tasks in the algorithm for a 32 atom Si calculation, using the pure orbital decomposition. It shows excellent speedup for **rhoofr** and application of the local part of the potential to the wavefunctions, due to the fact that the FFTs are done with no communication, completely in each processors local memory – inspection of the actual timing figures shows essentially 100% efficiency. Speedup of the non-local part of the computation is not as good due to some redundant computation carried out on each node. Unfortunately, since each node must do the calculations for all **g**, most of the work in **vofrho** must be carried out redundantly on each node, so that there is minimal speedup; however, since **vofrho** never requires more than about 10% of the CPU time, this is not a major handicap. The greatest challenge in the orbital decomposition is the parallel implementation of **ortho**. Good speedup is achieved only for small numbers of processors; the time required for **ortho** quickly approaches a minimum due to communication required when doing the parallel matrix multiplications. A pure spatial decomposition, on the other hand, shows good efficiencies for those parts of the code which involve computations strictly in real space or strictly in reciprocal space, but is much less efficient when transforming back and forth between the two (Fig. 2). The inefficiencies seen in those parts of the computation carried out purely in reciprocal space, such as the second subtask of **vofrho**, the second and third subtasks of **nonlocal**, and the sums over $\boldsymbol{g}$ in **nonlocal** and **ortho**, are due to load balancing problems; the decomposition of the FFT lattice results in an uneven division of the coefficients for very large numbers of processors, to the point where one node may have more than twice as many as some others; the nodes receiving a larger number of coefficients then become a bottleneck.

Thus both approaches begin to lose efficiency when the number of processors becomes large enough, but for different reasons. The spatial decomposition begins to suffer from load-balancing problems, and more importantly, it loses speed in the FFTs due to communication overhead. The orbital decomposition, on the other hand, reaches a bottleneck due to the communications when orthonormalizing the electronic orbitals. The orbital decomposition is somewhat faster for a given number of nodes, but it limits the number of nodes which can be applied to the problem to no more than half the number of orbitals - and it requires more memory due to redundant storage on different nodes. By combining the two approaches, it is possible to balance the decomposition so as take maximum advantage of the strong points of each approach. This hybrid parallel Car–Parrinello (HPCP) algorithm makes it possible to tune the decomposition for a given problem and a given number of nodes to get the maximum speedup. If the number of nodes available is limited, an optimal decomposition can be determined and used to minimize computational time. When the maximum number of nodes under orbital decomposition has been applied, it is possible to add spatial decomposition to apply an arbitrary number of nodes. We have found that, in fact, the optimal decomposition is usually *not* purely spatial or purely orbital, but a combination of the two.

4.1. The hybrid decomposition

The HPCP technique divides the computing nodes into groups; each group is assigned a subset of the electronic orbitals, and the computations on these orbitals are further subdivided spatially among the nodes within the group. The groups are chosen in such a way that the members can communicate with each other during the computation without interfering with the communications among members of other groups; they are compartmentalized to eliminate message contention during most of the computation. In addition, the nodes are arranged so that equivalent nodes - that is, nodes which have been assigned equivalent subsets of the expansion coefficients - in different groups can be mapped into a set of independent rings with as few shared communications links as possible. In this paper, we concern ourselves only with the details of implementation on the Intel Paragon and the Touchstone Delta, two multiple instruction, multiple dataset (MIMD) architectures with a mesh interconnect communication network. Implementation on other architectures with higher dimensional communication networks such as the T3D, which uses a 3D toroid communication interconnect, or on the iPSC/860 or nCUBE/2, which use the hypercube interconnect, is straightforward. For instance, the subgroups chosen on the T3D might be "planes" of processors within the 3D lattice.

With the mesh interconnect, the computer is viewed as a two-dimensional set of nodes, each with a connection to 4 neighbors on the North, East, West, and South, with the exception of those nodes on the edges of the mesh. For the purpose of mapping HPCP onto the nodes, the mesh is viewed as a 2D mesh of 2D submeshes. Fig. 3 gives a schematic picture of the three types of decomposition on a mesh computer for an example problem involving 32 orbitals; a purely orbital decomposition on the left, with each node responsible for all computations on two orbitals, a purely spatial decomposition on the right, where each node is responsible for approximately one sixteenth of the work on all 32 orbitals, and in the center a hybrid decomposition where the 4×4 mesh is decomposed into a 2×2 set of 2×2 submeshes, each submesh is responsible for 8 orbitals, and each subnode is responsible for approximately one fourth of the coefficients for those 8 orbitals. The operations which were carried out on a single node in the pure orbital decomposition are now carried out within the submesh by all the subnodes working in parallel. Communications which originally took place between individual nodes now

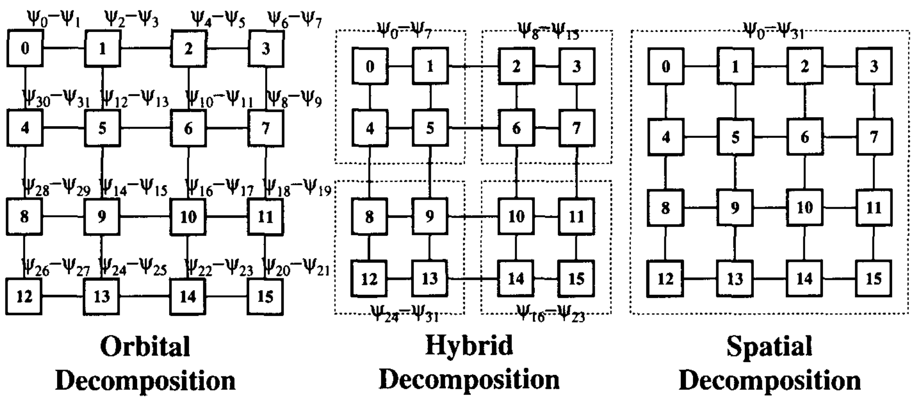

Fig. 3. Three possible data decompositions for a 16 Si atom simulation on 16 nodes. In the purely orbital, each node is responsible for 2 out of 32 orbitals. In the purely spatial, each node is responsible for part of the computation on all 32 orbitals. In the hybrid, each node is a member of a submesh, responsible for part of the computation on 8 of the 32 orbitals

pass between equivalent nodes within the submeshes. This has the effect of reducing communication time in the orthonormalization procedure considerably.

The next question, then, is how the coefficients will be assigned to the various subnodes within each submesh. Since the calculations for each plane-wave are identical, with the exception of the $\boldsymbol{g} = \boldsymbol{0}$, it is not particularly important which node contains which coefficients. Also, it is not important which parts of the real-space simulation cell are assigned to each node. However, there are several other considerations. First: the partition must be chosen so that the parallel FFTs can be done in an efficient manner. Second: the number of coefficients assigned to each subnode should be roughly equal to balance the load. Third, and most important: since we have chosen to include only the Γ point, the coefficients c^n_{-g} are actually just the complex conjugates of c^n_g, reducing the amount of storage required by half; in order to maintain this advantage, the partition must be chosen so that it is not necessary for different nodes to maintain consistent values of the coefficient for a given positive/negative plane-wave pair; that is, the elements of the FFT array in reciprocal space corresponding to the positive and negative plane-waves *must reside in the same node's memory*.

While it is certainly possible to implement true 3D parallel FFTs, in the case of a multi-dimensional FFT it is simpler and usually more efficient [18–20] to implement the 3D FFT as a series of 1D FFTs in the x, y, and z directions combined with data transpositions (Fig. 4). We have chosen to partition the data so that in reciprocal space, the entries for the z dimension are stored contiguously in local memory, and the x and y dimensions are decomposed across the nodes; thus, each node has a set of one-dimensional columns on which to work when doing the one-dimensional FFTs. The exact nature of this decomposition is determined by the second and third requirements mentioned above. A straightforward partitioning on a 4×4 submesh might be done as in Fig. 5a; this would make data transpositions quite simple, but would lead to major load-imbalance problems due to the fact that most of the entries in the FFT array in reciprocal space are actually zero. Only those plane-waves within the cutoff energy are actually used in the calculation; they fill only a relatively small region (Fig. 6) within the actual FFT array. It is this *sphere of active plane waves* within the FFT array which must be evenly divided, if the computations in reciprocal space are to be evenly divided among nodes. So the simple partition is discarded in favor of an *interleaved* partition (Fig. 5b), which results in a roughly equal division of the active plane-waves among the subnodes.

When doing a standard one-dimensional FFT of an array f with length L indexed from f_0 to f_{L-1}, the values of f_n in the array in real space correspond to values of some function f for equally-spaced values of some variable x, arranged in ascending order. When the array is transformed into reciprocal space, we are left with a new array F whose entries F_n correspond to the intensities of various frequencies $n\omega$ in a Fourier expansion of the function f. They are not, however, arranged in simple ascending order; rather, $F_0 = F(0)$,

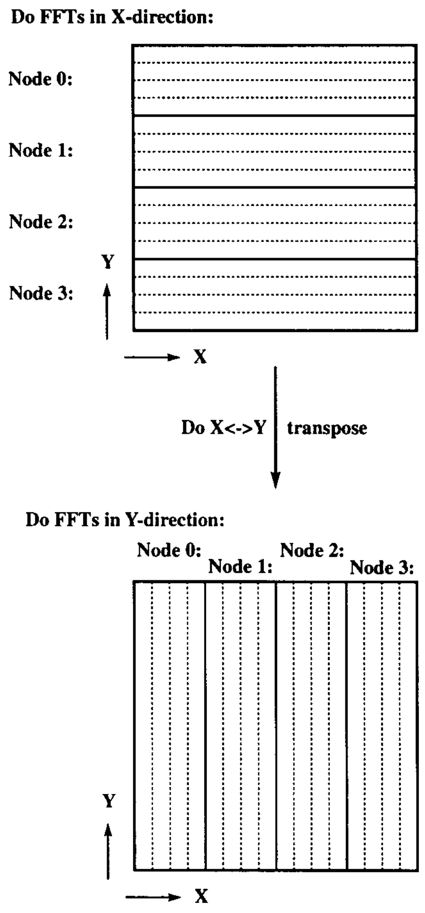

Fig. 4. Data-transpose algorithm for a two-dimensional parallel FFT. First one-dimensional FFTs are applied in the x-direction, then the matrix is transposed, then one-dimensional FFTs are applied in the y-direction. All FFTs are computed strictly in local memory. Communication is done only in the matrix transpose

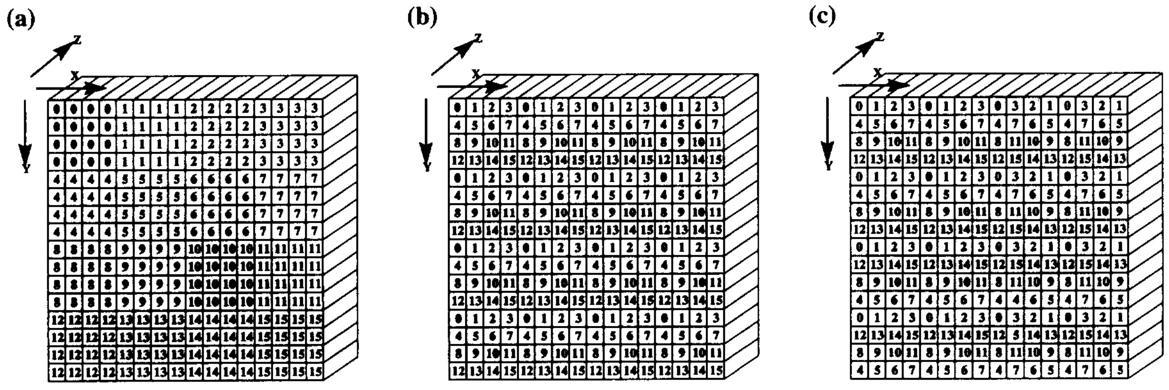

Fig. 5. (a) Simple, inefficient partitioning of the 3D FFT array across nodes; each node gets 16 columns in the z-direction, but some nodes will have few or no "active" plane waves assigned to them. (b) The interleaved partitioning assures that each node will get a reasonable share of the "active" plane waves, but does not address the problem of memory locations for positive-negative plane wave pairs. (c) The final partitioning

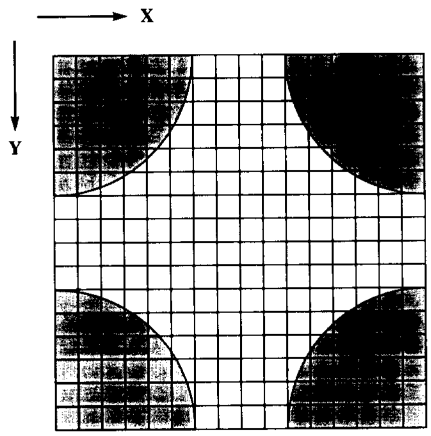

Fig. 6. An x–y projection of the FFT array showing the "active" elements in the array. Only those g falling within a cutoff radius determined by E_{cut} have coefficients with non-zero values; they take up the 8 "corners" of the array cell

$F_n = F(n\omega)$ for $0 < n < L/2$, and $F_n = F((n-L)\omega)$ for $L/2 \leq n < L$. Hence negative frequency $-m\omega$ maps to array location F_{L-m}. We must account for the fact that this will be the case in all three dimensions of our FFT array; positive plane wave (n_x, n_y, n_z) will map to negative plane wave (m_x, m_y, m_z) in a rather complicated manner depending upon the signs and values of n_x, n_y, and n_z; for instance if we use the simple interleaved partition suggested in Fig. 5b, plane wave $(1,2,3)$ would be stored in the local memory of node 9, but its negative $(-1,-2,-3)$ would map to $(15,14,13)$ and end up in the local memory of node eleven. Either it is necessary to double the storage for coefficients and determine a way to maintain coefficients for positive and negative plane waves as complex conjugates, or it is necessary to choose the data decomposition so that they are both stored in the same node's memory. The problem is simplified considerably if one looks at it in terms of the values of the plane waves rather than the partitioning of the FFT array itself. If node p is at location (i,j) in an $R \times C$ submesh, then those plane waves with $|n_x| \bmod C = j$ *and* $|n_y| \bmod R = i$ should be assigned to p. Assigning coefficients to nodes according to the absolute value of n_x and n_y forces the decomposition to satisfy the third condition, since *all* values in the z dimension are known to be in local memory already. A simple example of the final decomposition is shown in Fig. 5c.

4.2. The FFT calculations

Once the partition has been made, the FFT is straightforward. For simplicity, we consider only the transform from reciprocal space to real space; the reverse is analogous. Each node in the submesh begins with a subset of columns in the z dimension; it performs the one dimensional FFTs on these, then begins preparing to transpose the data so that it will have a subset of columns in the y dimension. The data is packed into a set of contiguous buffers so that the data which will remain on the node is placed in the "first" buffer, the data which needs to be transmitted to the node immediately "beneath" it goes in the next buffer, the data for the node "beneath" that one goes in still the next buffer, and so on; when the "bottom" of the mesh is reached, it wraps back to the top row in a toroid-fashion. Once the data is packed, a series of messages are passed along each column of subnodes; after the first message, each node has the data it requires from the node directly above it, as well as the data which was already in local memory. Each node retains the buffer which was meant for it, passes on the buffers which were meant for the nodes "below" it, and receives a new set of buffers from the node "above" it. After all the buffers have been sent, each node will have the data necessary to reconstruct the FFT array, with a subset of the columns in the y dimension in local memory.

This procedure is shown schematically in Fig. 7. The buffers B_{ij} are contiguous in memory so that the

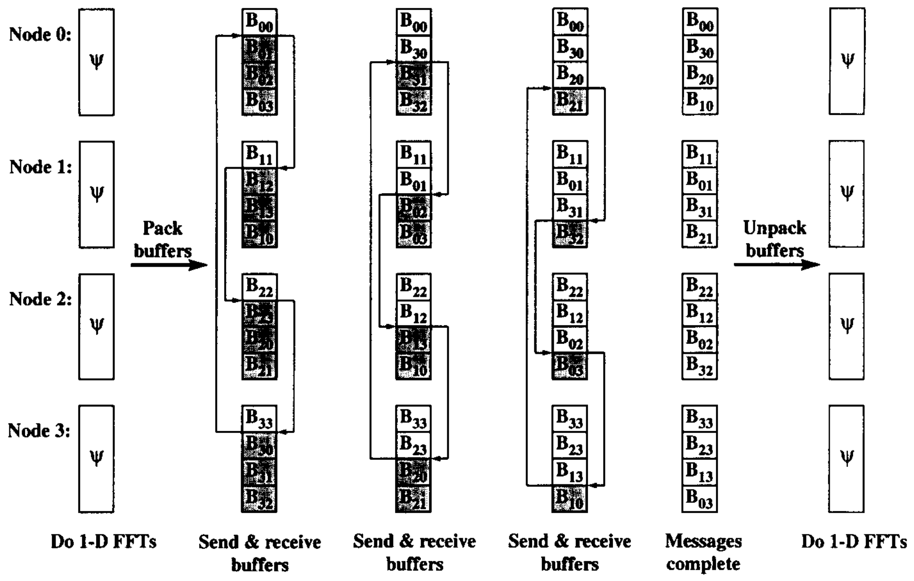

Fig. 7. Each node packs message buffers in memory so that it may successively send and receive smaller messages, each time receiving part of the data necessary for it to continue the next step in the algorithm, and also storing and forwarding to other nodes data they require, without introducing a great deal of message contention

messages, once packed, may be sent without any further data movement. Buffer B_{ij} is the data on node i which must be transmitted to node j. At each iteration, only the shaded buffers are transmitted to the next node. We use this store-and-forward technique because the software "bandwidth" on the Touchstone Delta, i.e. the amount of data which can be transferred from local memory out to the message network per unit time, is sufficiently close to the hardware bandwidth that it is possible to swamp the message backplane and degrade communications. The store-and-forward technique reduces all communications to near-neighbor messages, eliminating this possibility. On the Paragon, however, the hardware bandwidth is almost an order of magnitude greater than the speed with which any particular node can move data from its local memory out onto the network, so it is almost impossible to swamp the backplane; it may be that direct messages will be faster under these conditions.

Once the FFT array is reassembled, each node performs the appropriate one dimensional FFTs on the subset of the columns in the y dimension in its local memory. When these are done, the nodes again pack a set of message buffers, but this time the messages will be passed *horizontally* along each row of the submesh in order to transpose the y and x coordinates; when the messages have been passed and the buffers unpacked, each node will have a subset of the columns in the x dimension in local memory. Appropriate FFTs are performed, and the three dimensional parallel FFT is complete. The FFT back to reciprocal space simply performs the same operations in reverse order, doing the x FFTs first, transposing x and y, doing the y FFTs, transposing y and z, and finally doing the z FFTs. An overall schematic of the FFT showing the data flow during the transpose operations is shown in Fig. 8.

4.3. Global summations

Global summation is a parallel operation whereby the sum of the values stored in some variable or variables on different nodes is calculated.

In the HPCP code, three different global summations are needed. Referring to the hybrid decomposition diagram in Fig. 3, those are: (1) a standard global summation, where all the nodes, zero through fifteen, contribute to the sum; (2) a global summation *over all nodes within a submesh*, for instance, only summing up

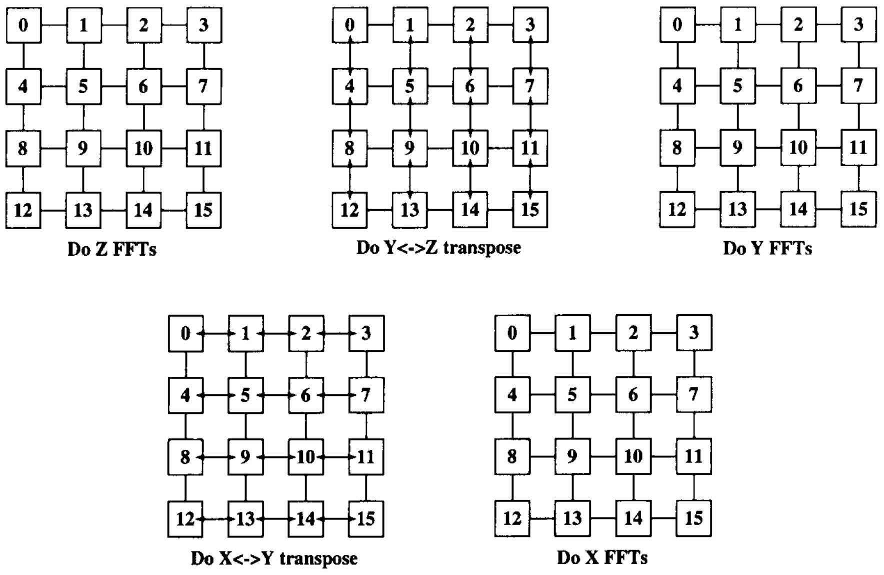

Fig. 8. The parallel 3D FFT algorithm; 1D FFTs are applied successively in each dimension, with transpositions of the data array between. The individual rows and columns of nodes may carry out the transpositions of their local data independently, greatly increasing bandwidth and efficiency

values of the variable stored on nodes two, three, six, and seven; and (3) a global summation *over equivalent nodes in all the submeshes*, for instance over nodes five, seven, thirteen, and fifteen.

Standard library calls on most parallel computers can do the first type of summation. The other two types of sums need to be specially coded. We have used as a basis for our global summations the technique suggested by Littlefield and van de Geijn [31], modified for the specific circumstances. The general technique involves independent sums along the rows (or columns) of the mesh, leaving the first node in the row (or column) with the sum of the values along the row (or column). Then a summation is done along the first column (or row), leaving the node in the (0,0) position with the result. The communications pattern is then reversed, as the result is broadcast out along the first column (or row) and then independently along each row (or column). If properly done, there is no message contention and the time required for completion scales as $\log_2 P$, with P the number of nodes. Doing this *within a submesh* is straightforward; there is no possibility of message contention, since no node within the submesh ever needs to send a message outside the boundaries of the submesh.

Doing summations over equivalent nodes, however, presents a problem; there will inevitably be message contention for large enough numbers of processors. It can be minimized, however, by taking advantage of the fact that it is arbitrary whether the first phase of the summation is done along the rows or the columns. If all sets of equivalent nodes do their summations with identical ordering of messages, a great deal of contention will be introduced (Fig. 9a). If, on the other hand, every other set, selected according to a "checkerboard" coloring, does the first stage along the *rows*, message contention is reduced by half (Fig. 9b).

4.4. Matrix multiplication

In order to perform the iterative orthonormalization efficiently, it is necessary to have an efficient parallel matrix multiplication routine. The matrix multiplication used for the pure orbital decomposition can be extended to make efficient use of the hybrid node layout, increasing the effective bandwidth by roughly the square root of the number of nodes in each submesh. To illustrate this, it is necessary to review the way in which the matrix multiplication was implemented in the earlier, pure orbital decomposition code [16].

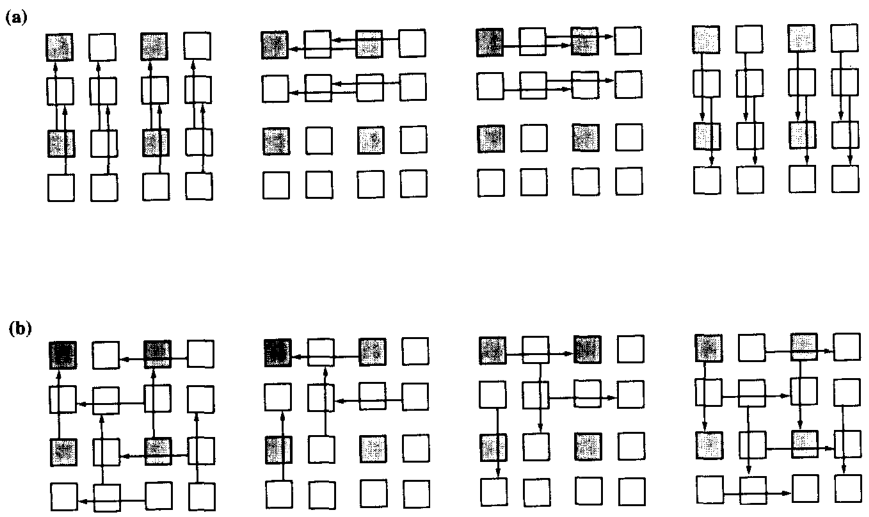

Fig. 9. (a) All sets of nodes do global sums in the same order; first along columns, then along rows. One set of equivalent nodes is highlighted for emphasis. In each place where two parallel message indicators overlap, there is contention for a communication link. (b) If the nodes within a submesh are colored "red-black" like the pattern of a checkerboard, and the "red" nodes do their sums first along the rows while the "black" nodes do their sums first along the columns, the message contention is reduced by half

First, a "ring" was mapped into the underlying communication topology so that each node had a "neighbor" on its "left" and its "right," to which it had a direct, unshared communications link. The coefficient array was divided up among the members of this ring so that each node had an equal number of rows. Doing the large matrix multiplications when evaluating Eqs. (3.19) and (3.20) required that each node use the rows of the coefficient matrices stored in its local memory to calculate a subblock of the result matrix, pass its rows along to the next node in the ring, and receive the next set of rows from the previous node in the ring. The algorithm was described in more detail, with schematics, in Ref. [16].

This parallel matrix multiply was free of contention and maintained load balancing, but its efficiency was greatly limited by the available bandwidth between nodes. Its performance dropped off rapidly as the number of nodes increased, due to time spent waiting for the messages to get around the ring. As an example, results of calculations on a 64 Si atom system on the Paragon and the Delta are shown in Fig. 10. The time for each is well described by the relation $t = a + b/P$, where P is the number of nodes and a is the time spent in communications. This baseline is independent of the number of nodes due to the fact that as the number of nodes increases, the number of messages also increases but the *size* of the messages decreases in exact proportion; the total amount of data that each node is required to send and receive is independent of the number of nodes. The baseline for the Paragon is less than half that of the Delta, owing to the former's greater node-to-node communication bandwidth.

A hybrid parallel matrix multiply greatly alleviates this communication bottleneck. Each node within a submesh has a subset of the coefficients for some subset of the orbitals. If equivalent processors from the submeshes are mapped into independent rings, each can do a matrix multiply with its own submatrix; the final result matrix can be obtained by doing global sums within each submesh of the result matrices produced by each node (Fig. 11).

4.5. Parallel algorithm for ***ortho***

Once the parallel matrix multiplication has been implemented, the ortho routine is relatively simple. The arrays **b** and $\mathbf{X}^{(0)}$ (Eqs. (3.19) and (3.20)) are calculated by multiplying the coefficient matrices by their

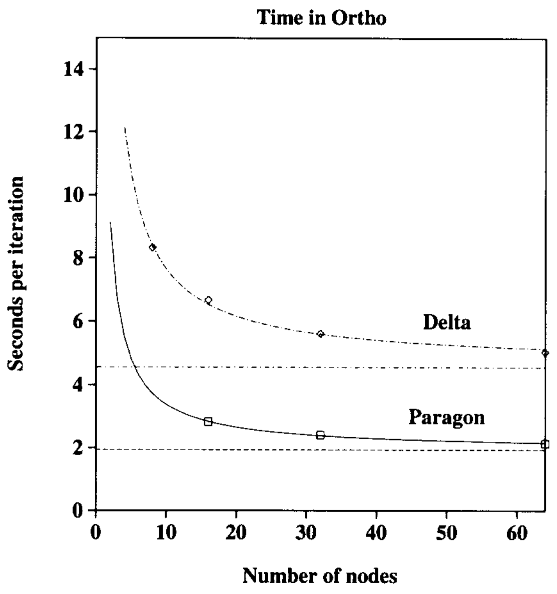

Fig. 10. CPU time spent in the iterative orthogonalization routine on the Delta and Paragon computers in a simulation of 64 Si atoms using pure orbital decomposition. As the number of nodes used in the computations is increased the computational time decreases but the communications time stays the same. The lower baseline for the Paragon curve demonstrates the higher communication bandwidth, which reduces the time spent in communications

transposes; the data is already properly laid out for the matrix multiplication technique described above. The array $\mathbf{X}^{(0)}$ is constructed according to Eq. (3.19) by multiplying the new matrix of coefficients for time $t+\delta t$, which are not orthonormalized, by its own transpose. The array **b** (Eq. (3.20)) is constructed by multiplying this matrix by the transpose of the matrix of coefficients for the current time t, which are already orthonormalized. The iteration involves similar matrix multiplications of arrays $\mathbf{X}^{(0)}$ and **b**, or linear combinations thereof, by the transposes of other linear combinations; thus the same matrix multiplication technique can be applied to the calculations within the iteration loop, without need for any matrix transpositions. These matrix multiplications within the iteration loop are carried out redundantly on each set of equivalent nodes, since each node in the submesh will need a copy of the result matrix $\mathbf{X}^{(k)}$ to correct the new array of coefficients; however, since the amount of work required for these is $O(N^3)$ rather than the $O(N^2M)$ required to calculate **b** and $\mathbf{X}^{(0)}$ $(M \gg N)$, the redundant calculation has little effect on the overall timing of **ortho**.

The **ortho** routine has a decided advantage over the GS technique when doing large problems and decomposing by orbitals; the amount of data communication it requires does not grow with the number of nodes, whereas the GS technique's communication requirements increase as the number of orbitals per node decreases. In the GS procedure the nodes do a sequential loop over all orbitals; the node which "owns" the orbital normalizes it, then *broadcasts* it to all the other nodes, who then orthogonalize to it any of those orbitals they "own" which have not already been so treated. As such, the algorithm requires N broadcasts, each of which requires $\log_2 P$ messages to be sent if there are P nodes. For a problem with N orbitals, M coefficients, and P nodes, the communication requirements for GS are then: $O(NM\log_2 P)$. The **ortho** routine, on the other hand, requires three large matrix communications like those described in Section 4.4, each of which requires P messages of length MN/P (the time for the smaller $N \times N$ matrix multiplications is swamped by these), implying O(NM) communications regardless of the value of P. Of course, in the hybrid implementation, P refers to the number of *submeshes*, as this determines how many messages must be sent. A purely spatial decomposition would not require any of the communication described here – only a series of global sums to determine the orbitals' overlaps.

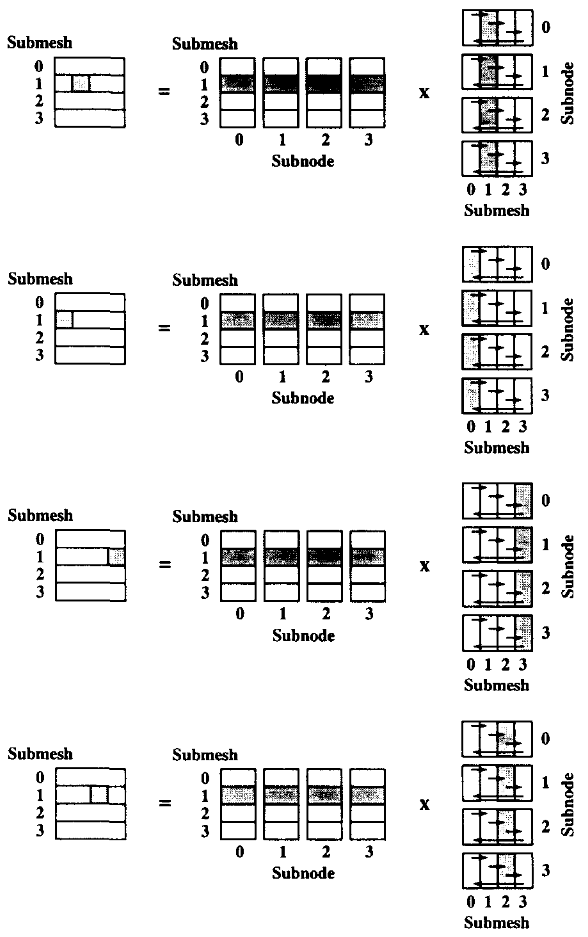

Fig. 11. The hybrid parallel matrix multiplication algorithm. Each node carries out an independent matrix multiplication of the parts of the matrices in its local memory, then passes its subblock of the second matrix to the next node in the ring of equivalent nodes in the other submeshes; arrows indicate direction of data movement between nodes of each ring. The shaded blocks in the result matrix indicate the part being calculated at each iteration in submesh 1; the shaded blocks in the matrices being multiplied indicate the part of these matrices resident in memory on each subnode of submesh 1 at each iteration. *Each* node in the submesh keeps a copy of the indicated strip of the result matrix; when the independent matrix multiplications are done, a global summation of the values in that strip of the result matrix is carried out within each submesh, leaving each subnode with the final result

4.6. Parallel algorithm for **rhoofr**

The algorithm for **rhoofr**, which calculates the total electronic density within the simulation cell, is quite simple. Each submesh loops over the orbitals assigned to it, placing the coefficients for each into the proper locations in the FFT array and doing inverse FFTs to get the value of the electronic wavefunction in real space; the entries are then squared, scaled by the appropriate occupation number f_n, and accumulated in the array **rhoe**. When this loop is completed, independent global sums of **rhoe** are calculated *over equivalent nodes*, leaving each node with the total electronic density in that subregion of the simulation cell for which it is responsible.

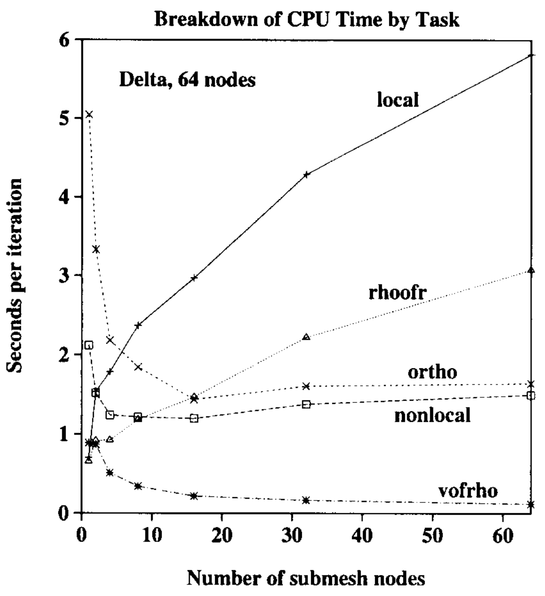

Fig. 12. Time spent on the various subroutines of the HPCP algorithm vs. the number of nodes in each submesh, in a simulation of 64 Si atoms. The timings are from the Delta, using 64 nodes total. One node per submesh corresponds to a pure orbital decomposition, 64 nodes per submesh corresponds to a pure spatial decomposition

5. Some performance numbers

The HPCP code makes it possible to "tune" the decomposition for a particular problem and given number of nodes to minimize the time required for the calculation. To demonstrate this, we describe below several test runs done on both the Delta and Paragon computers. The calculations were done on systems of Si atoms in the crystalline arrangement, using s and p non-locality BHS pseudopotentials with the KB factorization, and an energy cutoff for the plane wave expansion of 12 Ry. Fig. 12 shows timings from calculations done using 64 nodes on the Touchstone Delta, starting with a purely orbital decomposition (1 node per submesh) and increasing the number of nodes per submesh up to 64 nodes, giving a purely orbital decomposition. The major subroutines described above were timed separately. The behavior of **rhoofr**, **local**, and **ortho** in particular are of interest and are described in more detail below.

local represents the time required to apply the local part of the pseudopotential; it requires two FFTs for each orbital. For each orbital in turn, the coefficients are placed into the FFT array, an inverse FFT is performed to get the value of the wavefunction in real space, the real space wavefunction in multiplied by the potential calculated in **vofrho**, and a forward FFT is done, yielding the values of the "local" force on the electronic coefficients. **rhoofr** requires only one FFT per orbital, as described in Section 4.6. The rapid increase in time required for these two routines is due to the loss of efficiency in the parallel FFTs. The actual amount of computation per node does not change, but the communication time increases as more nodes are involved in each FFT calculation. It is impossible for any parallel FFT to be more efficient than simply dividing up the FFTs and doing them independently on separate nodes as is the case in the orbital decomposition. Clearly, for these two tasks, the orbital decomposition is superior.

On the other hand, the timing in **ortho** improves rapidly as the number of nodes per submesh increases. The reason is that the amount of communication required for the matrix multiplications decreases as the number of submeshes decreases. For a purely spatial decomposition, no communication is required to do the multiplication of the submatrices; the only communication required is the final global sum to get the total values in the result matrix. For a hybrid decomposition, as the number of submesh nodes increases, the number of submeshes

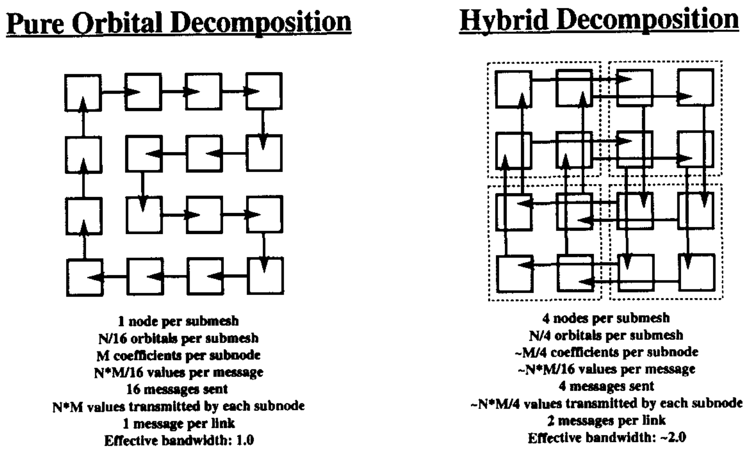
Pure Orbital Decomposition
Hybrid Decomposition
1 node per submesh
N/16 orbitals per submesh
M coefficients per subnode
N*M/16 values per message
16 messages sent
N*M values transmitted by each subnode
1 message per link
Effective bandwidth: 1.0
4 nodes per submesh
N/4 orbitals per submesh
~M/4 coefficients per subnode
~N*M/16 values per message
4 messages sent
~N*M/4 values transmitted by each subnode
2 messages per link
Effective bandwidth: ~2.0

Fig. 13. Breakdown of communications requirements and effective bandwidth for **ortho** in a purely orbital and a hybrid decomposition. The hybrid decomposition increases the speed of the algorithm by reducing the number of messages required by a factor of four while only decreasing the bandwidth available to each node by a factor of two.

Table 2
Timing comparisons of various simulations of 512 Si atoms

Reference	Computer	Nodes	Decomposition	E_{cut} (Ry)	s/step
Nelson et al. [17]	nCUBE/2	1024	Spatial	8.0	11677
Brommer et al. [14]	CM-2	64K	Spatial	12.0	3000
Present work	Delta	512	Hybrid	12.0	250

decreases, and the effective bandwidth increases roughly as the square root of the number of nodes in each submesh. This behavior is illustrated in Fig. 13 for a system with N orbitals and M coefficients. This analysis is born out by the actual timings gathered; when the number of nodes is fixed at 64 and the number of subnodes per submesh increases from one to four, the time required for ortho drops from 5.05 seconds to 2.18 seconds – slightly better than the factor of two which was expected. As the number of nodes per submesh is increased further, the time spent in ortho begins to be dominated by the communications required for the final global sum in each matrix multiplication. No improvement in timing is obtained beyond sixteen subnodes.

Another advantage of the HPCP algorithm is that it allows more nodes to be applied to the problem than could be done with the purely orbital decomposition. For example, a system of 64 Si atoms has 128 orbitals; the largest number of nodes which could be applied to this in the pure orbital decomposition is 64. Using the HPCP code, the number can then be expanded; instead of 64 nodes we can, for example, use 64 submeshes, each with as many subnodes as we wish. In this case, the effective bandwidth for the matrix multiplications will again increase roughly as the square of the number of processors, though for a different reason. If we increase the computational mesh from an 8×8 mesh to a 16×16 mesh divided into 2×2 submeshes, the communication pattern among equivalent subnodes is identical; each subnode will see itself as a member of an 8×8 mesh made up of itself and the equivalent subnodes in the other submeshes. The number of messages required when doing the matrix multiplications remains the same, and each subnode will be sharing a communication link with one other (cf. Fig. 13), but the messages will be roughly one-fourth the *size* of those in the 8×8 mesh, so the overall speed will increase by roughly a factor of two. Again, the actual timings gathered bear this out; the time for **ortho** on an 8×8 mesh is 5.05 seconds, and on a 16×16 mesh divided up into 2×2 submeshes, it is 2.05 seconds.

From Fig. 12, it is apparent that most of the speedup obtained in **ortho** by increasing the number of subnodes

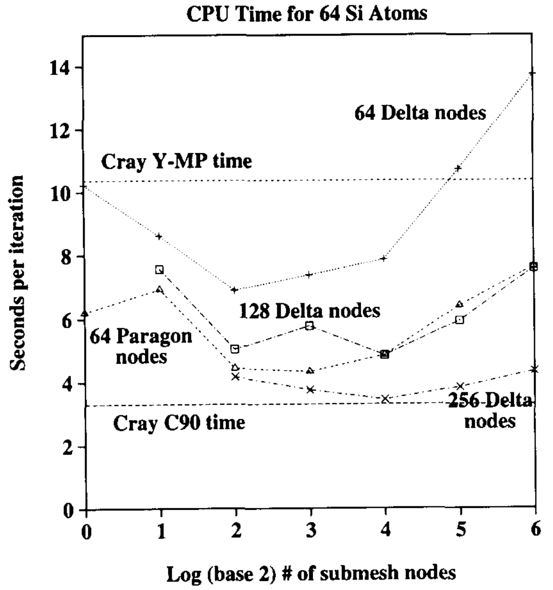

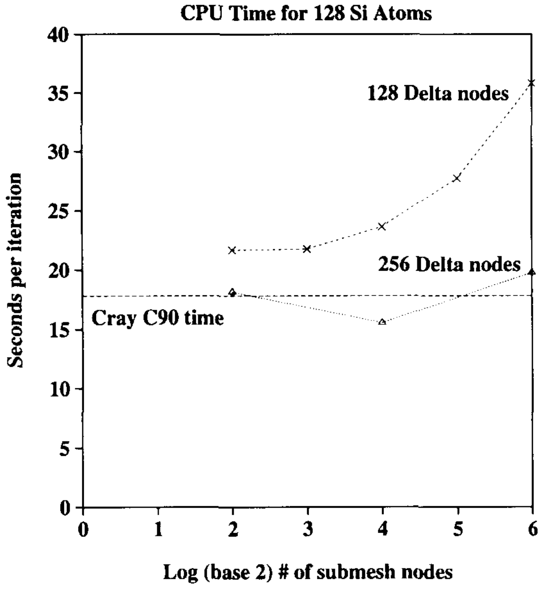

Fig. 14. Total time per iteration for a system of 64 Si atoms on four different architectures. The two horizontal lines give timings for the Cray Y-MP and the Cray C90; the curves represent timings for different numbers of nodes on the Touchstone Delta and the Intel Paragon. Timings were done with 64, 128, and 256 nodes of the Toucshtone Delta and with 64 nodes of the Intel Paragon. The curves indicate how the time per iteration changes with the decomposition; the x axis is the $\log_2$ of the number of nodes per submesh

Fig. 15. Total time per iteration for a system of 128 Si atoms on two different architectures. The horizontal line gives the time per iteration on the C90; the curves represent timings for 128 and 256 nodes of the Toucshtone Delta. Again, the x axis is the $\log_2$ of the number of nodes per submesh

is achieved before the time spent in **local** and **rhoofr** increases significantly, with a minimum for the overall time when the number of nodes per submesh is four or eight. The optimal decomposition is one which is neither purely spatial nor purely orbital, but a combination of the two. Fig. 14 shows the total time per iteration of the CP algorithm in a simulation of 64 Si atoms. It is possible to outperform a highly optimized sequential version of the CP algorithm running on the Cray Y-MP using only 64 nodes of the Delta, and to almost match the times on the Cray C90 using 256 nodes, even for a problem as small as 64 Si atoms. Fig. 15 shows a similar comparison for a larger system of 128 Si atoms. As the size of the problem increases, the parallel algorithm does even better; it is possible to outperform the C90 using 256 nodes on the Delta, decomposed as a 4×4 mesh of 4×4 submeshes.

The main motivation for parallel implementations of the CP algorithm is to open the possibility of simulating systems with more atoms than are possible with existing and foreseeable sequential computers. As such, most groups that have implemented CP or similar electronic-structure calculations on a parallel supercomputer have reported timings for a few large systems. Both Nelson et al. [17] and Brommer et al. [14] report timings for a system of 512 Si atoms; in order to make a comparison, we have done likewise on the Touchstone Delta. Nelson et al. implemented their code on an nCUBE 2 with 1024 nodes located at the San Diego Supercomputer Center; the calculation they timed was 512 Si atoms with one k-point and an 8-Ry energy cutoff; their time per iteration was ~12000 seconds [17]. Brommer et al. implemented their code on the Connection Machine CM-2, a Single Instruction, Multiple Data parallel computer. Their CM-2 was equipped with 65536 bit-serial processors and 2048 64-bit floating point units. Their simulation was done on 512 bulk Si atoms with a 12-Ry energy cutoff. Estimated by reading from a log–log scale graph (Fig. 9 in Ref. [14]), the time per iteration was ~3000 seconds. For our calculation, we used 512 nodes of the Touchstone Delta. The nodes were mapped as a 4×8 mesh of 4×4 submeshes, and the time per iteration was 250 seconds. A concise list of times is given in Table 2. It must be stressed that the other groups may not have implemented precisely the same algorithm; for instance Nelson et al. actually implemented the first-order equation of motion approach of Williams and Soler [32] which, while very similar to CP, is not identical.

6. Conclusions

The implementation of the Car–Parrinello algorithm on scaleable massively parallel computers permits simulations of systems too large to simulate on conventional vector supercomputers. Hybrid spatial and orbital decomposition of the problem makes it possible to achieve substantially higher throughput with a given number of processing nodes; neither a purely spatial nor a purely orbital decomposition gives optimal speedup.

Acknowledgements

We thank Prof. Roberto Car for making his CRAY code available to us. We are indebted to Dr. Arthur Smith for various helpful discussions. Thanks also to Dr. Rick Kendall and Dr. Rik Littlefield of Battelle Pacific Northwest Labs for various helpful discussions on parallel implementations in particular on the Delta computer, and to Dr. Larry Snyder and his research group at the Computer Science and Engineering Department of the University of Washington for various helpful discussions and suggestions on parallel computing in general. And finally, thanks to Greg Mills for his suggestions which led to the data decomposition used for the parallel FFTs.

This research has been supported by the Department of Energy's Computational Science Graduate Fellowship Program (JW) and by NSF-CARM grant CHE-9217294. Computer time was made available on the Delta by PNL-Battelle in Richland, WA, on the Paragon at Oak Ridge National Labs through the National Energy Research Supercomputer Center at Lawrence Livermore National Labs, and on the Paragon and CRAY Y-MP8/684 by the San Diego Supercomputer Center.

References

[1] R. Car and M. Parrinello, Phys. Rev. Lett. 55 (1985) 2471.
[2] R. Car and M. Parrinello, in: Simple Molecular Systems at Very High Density, Vol. 186 of NATO Advanced Study Institute, Series B: Physics, eds. A. Polian, P. Loubeyre, and N. Boccara (Plenum, New York, 1988).
[3] R. Car and M. Parrinello, Phys. Rev. Lett. 60 (1988) 204.
[4] I. Štich, R. Car and M. Parrinello, Phys. Rev. Lett. 63 (1989) 2240.
[5] I. Štich, R. Car and M. Parrinello, Phys. Rev. B 44 (1991) 4262.
[6] D. Hohl and R. O. Jones, J. Non-Cryst. Solids 117 (1990) 922.
[7] G. Brocks, P. J. Kelly and R. Car, Phys. Rev. Lett. 66 (1991) 1729.
[8] M. C. Payne, I. Štich, R. D. King-Smith, J-S. Lin, A. De Vita, M. J. Gillan and L. J. Clarke, in: Computer Aided Innovation of New Materials, eds. by M. Doyama, J. Kihara, M. Tanaka and R. Yamamoto (Elsevier Science, Amsterdam, 1993) p. 101.
[9] K. D. Brommer, M. Needels, B. E. Larson and J. D. Joannopoulos, Phys. Rev. Lett. 68 (1992) 1355.
[10] W. Andreoni and P. Ballone, Phys. Scr. T 19A (1987) 289.
[11] D. Hohl, R. O. Jones, R. Car and M. Parrinello, Phys. Lett. 129 (1987) 540.
[12] P. Ballone, W. Andreoni, R. Car and M. Parrinello, Phys. Rev. Lett. 60 (1988) 271.
[13] I. Štich, M. C. Payne, R. D. King-Smith, J-S. Lin and L. J. Clarke, Phys. Rev. Lett. 68 (1992) 1359.
[14] K. D. Brommer, M. Needels, B. E. Larson and J. D. Joannopoulos, Comput. Phys. 7 (1993) 350.
[15] L. J. Clarke, I. Štich and M. C. Payne, Comput. Phys. Commun. 72 (1992) 14.
[16] J. Wiggs and H. Jónsson, Comput. Phys. Commun. 81 (1994) 1.
[17] J. S. Nelson, S. J. Plimpton and M. P. Sears, Phys. Rev. B 47 (1993) 1765.
[18] A. Gupta and V. Kumar, IEEE Trans. Parallel Distributed Systems 4 (1993) 922.
[19] D. C. Marinescu, Fourth Symposium on the Frontiers of Massively Parallel Computing, McLean, VA (IEEE Comput. Soc. Press, 1992) pp. 150-4.

[20] G. Angelopoulos and I. Pitas, Signal Proc. 30 (1993) 355.
[21] P. Hohenberg and W. Kohn, Phys. Rev. B 136 (1964) 864.
[22] W. Kohn and L. J. Sham, Phys. Rev. 140 (1965) A1133.
[23] G. B. Bachelet, D. R. Hamann, and M. Schlüter, Phys. Rev. B 26 (1982) 4199.
[24] L. Kleinman and D. M. Bylander, Phys. Rev. Lett. 48 (1982) 1425.
[25] H. C. Andersen, J. Chem. Phys. 72 (1980) 2384.
[26] S. Nosé, Mol. Phys. 52 (1984) 255; J. Chem. Phys. 81 (1984) 511.
[27] W. G. Hoover, Phys. Rev. A 31 (1985) 1695.
[28] J. P. Ryckaert, G. Ciccotti and H. J. C. Berendsen, J. Comput. Phys. 23 (1977) 327.
[29] N. Troullier and J. L. Martins, Phys. Rev. B 43 (1991) 8861.
[30] R. D. King-Smith, M. C. Payne and J. S. Lin, Phys. Rev. B 44 (1991) 13063.
[31] R. Littlefield, M. Barnett, D. Payne and R. van de Geijn, Global Combine on Mesh Architectures with Wormhole Routing, in: Proc 7th Intern. Parallel Processing Symposium, Newport Beach, CA, April 13-16, 1993.
[32] A. R. Williams and Soler, Bull. Am. Phys. Soc. 32 (1987) 562.